Asymmetric Roughness of Elastic Interfaces at the Depinning Threshold

Esko Toivonen,* Matti Molkkari, Esa Räsänen, and Lasse Laurson
Computational Physics Laboratory, Tampere University, P.O. Box 692, FI-33014 Tampere, Finland

(Received 23 December 2021; accepted 22 September 2022; published 18 October 2022)

Roughness of driven elastic interfaces in random media is typically understood to be characterized by a single roughness exponent ζ. We show that at the depinning threshold, due to symmetry breaking caused by the direction of the driving force, elastic interfaces with local, long-range, and mean-field elasticity exhibit asymmetric roughness. It is manifested as a skewed distribution of the local interface heights, and can be quantified by using detrended fluctuation analysis to compute a spectrum of local, segment-level scaling exponents. The asymmetry is observed as approximately linear dependence of the local scaling exponents on the difference of the segment height from the mean interface height.

DOI: 10.1103/PhysRevLett.129.175701

Introduction.—Driven elastic interfaces in quenched random media, including, e.g., domain walls in ferromagnets [1] and ferroelectrics [2], contact lines in wetting [3], and crack fronts in disordered solids [4], exhibit universal dynamical response to external driving forces. These features are linked to an underlying depinning phase transition between pinned and moving phases of the interface at a critical external force [5,6], originating from the interplay between quenched disorder, elasticity, and an external driving force. In addition to dynamical properties such as interface motion taking place in a sequence of avalanches exhibiting scaling [1,7], a key feature of elastic interfaces at the depinning threshold is their rough morphology [8]. The roughness of an elastic interface with a height profile $h(x)$ is typically understood to be characterized by a single roughness exponent ζ, e.g., by considering the scaling of the saturated mean squared interface width $W^2(L) \sim L^{2\zeta}$ with the system size L, or that of the two-point correlation function $C(x) = \langle [h(x' + x) - h(x')]^2 \rangle \sim x^{2\zeta}$ along the interface, averaged over pinned interface configurations [9].

This simple description assumes that a single roughness exponent sufficiently characterizes the pertinent properties of the system. Thus, this description does not account for any possible asymmetries of $h(x)$ with respect to, e.g., its mean value $\langle h \rangle$. However, many driven elastic interfaces in quenched random media exhibit local statistical properties and correlations that may greatly diverge from such a simple, symmetric picture. Consider as an example a dislocation line (with a rather peculiar nonlocal self-interaction kernel [10]) driven by an applied shear stress through a sparse set of precipitate particles acting as localized obstacles for dislocation motion [11,12]: the dislocation will bow out in between the precipitates while remaining pinned at them, resulting in noticeable differences between the appearance (e.g., magnitude of the local curvature) of dislocation line segments that have moved more or less than the average dislocation displacement (see, e.g., Fig. 3 of Ref. [12]). Hence, by looking at a pinned dislocation configuration at a scale comparable to the precipitate spacing, it is immediately clear which way the dislocation line is being driven by the stress. On the other hand, when observing such interfaces on length scales exceeding the disorder correlation length (as is usually done by construction in simple models of interface depinning), any possible asymmetry with respect to $\langle h \rangle$ is less apparent; see Fig. 1(a).

Here we show that even for scales well above the disorder correlation length where the interface roughness emerges as a consequence of weak or collective pinning [13], the roughness of elastic interfaces at the depinning threshold exhibits several asymmetric features, originating from the broken symmetry caused by the direction of the external driving force. Considering as an example system the long-range elastic string [14–16] (in what follows we will use the terms "string" and "interface" interchangeably), known to describe systems such as planar cracks [4,17,18], contact lines [3], and low-angle grain boundaries [19], we find skewed distributions of both the local interface height and the local elastic force; analogous results for local and mean-field elasticity are presented in Supplemental Material [20]. Analyzing interface segments on different scales conditioned on the deviation of the average segment height from the mean interface height and the average elastic force acting on the segment reveals clear trends in the segment height profiles. Hence, we employ detrended fluctuation analysis (DFA) [23,24] with a scale-dependent segmentation scheme [25] to analyze the scaling properties of such segments. The resulting scaling exponents α are found to converge in the limit of high order of the detrending polynomial, with the converged exponents exhibiting a clear dependence on the difference of the segment height and the mean interface height, and on the

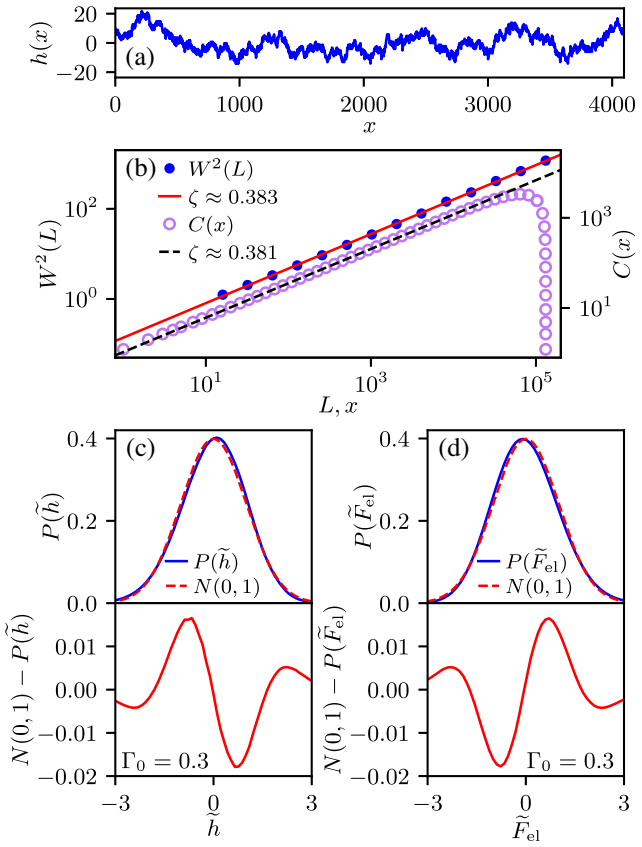

FIG. 1. (a) Example of a rough interface configuration $h(x)$ for $L = 4096$. (b) Roughness exponent ζ measured from the scaling of $W^2(L)$ and $C(x)$ (see text). (c) Distribution $P(\tilde{h})$ of the scaled local interface height $\tilde{h} = [h(x) - \langle h \rangle]/\sigma_h$ (top), and the difference between $P(\tilde{h})$ and standard normal distribution $N(0, 1)$ (bottom). (d) Distribution $P(\tilde{F}_{el})$ of the scaled local elastic force $\tilde{F}_{el} = F_{el}/\sigma_{F_{el}}$ (top), and the difference between $P(\tilde{F}_{el})$ and standard normal distribution $N(0, 1)$ (bottom).

average elastic force. The average values of these local exponents tend toward the roughness exponent ζ in the large-scale limit. Thus, instead of the classical description in terms of a single roughness exponent ζ, our results show that elastic interfaces at the depinning threshold should be characterized by a spectrum of local, segment-level exponents which depend on quantities like the deviation of the segment height from the mean interface height and/or the average elastic force acting on the segment.

Model: Long-range elastic string.—We perform extensive simulations of a discretized version of the long-range elastic string in a quenched random medium. The local total force acting on the interface element i located at $x = x_i \equiv i$ (with i an integer from 0 to L) along the interface $h(x) = h(x_i) \equiv h_i$ is

$$F(x_i) = F_{el}(x_i) + \eta(x_i, h_i) + F_{ext}, \tag{1}$$

where the first term on the rhs, $F_{el}(x_i) = \Gamma_0 \sum_{j \neq i} [(h_j - h_i)/|x_j - x_i|^2]$ (with Γ_0 the stiffness of the interface), represents the long-range elastic interactions, η is uncorrelated quenched disorder, and F_{ext} is the external driving force [4]. The parallel dynamics of the interface is defined in discrete time t by setting the local velocity $v(x_i, t) \equiv h(x_i, t + 1) - h(x_i, t) = \theta[F(x_i)]$, where θ is the Heaviside step function. We employ quasistatic constant velocity driving which keeps the interface in the immediate proximity of the depinning threshold, such that avalanches are triggered by increasing F_{ext} just enough to make exactly one interface element unstable [that is, $F(x_i) > 0$ for some i] whenever the previous avalanche has ended. During an avalanche, F_{ext} is decreased at a rate proportional to the instantaneous avalanche velocity, $\dot{F}_{ext} = -K/L \sum_i v_i(t)$, where K is a parameter controlling the cutoff of the avalanche size distribution [4]. To collect data for studying the interface roughness, we simulate the system according to the above protocol and store interface configurations $h(x)$ from the steady state at regular intervals separated by long enough interface displacements such that consecutive interface configurations are uncorrelated. The parameters are set to $L = 4096$, $K = 0.0033$, and $\Gamma_0 = 0.3$ unless stated otherwise, but we consider also different L's up to $L = 131\,072 = 2^{17}$, and adjust K accordingly to approximately fix the ratio of the correlation length (maximum lateral extent of avalanches) and L.

Skewed distribution of interface heights.—Figure 1(a) shows an example of an interface profile $h(x)$ for $L = 4096$, illustrating the typical rough morphology one observes above the length scale of the disorder correlation length (which here equals 1). Our interfaces follow the standard scaling picture in that the roughness exponent ζ, estimated from $W^2(L)$ and $C(x)$ in Fig. 1(b) for system sizes up to $L = 2^{17}$, is very close to the literature value of $\zeta \approx 0.385$ [9]. However, a closer look reveals the first signature of asymmetry in the statistical properties of the $h(x)$'s: The distribution of local interface heights $P(\tilde{h})$, where $\tilde{h} \equiv [h(x) - \langle h \rangle]/\sigma_h$ [with the standard deviation σ_h calculated over the whole dataset of $h(x) - \langle h \rangle$ values], exhibits a small but clearly nonzero negative skewness [26] of -0.183, and hence deviates from the standard normal distribution $N(0, 1)$ [Fig. 1(c)]. Similar conclusions can be made by considering the distribution of local elastic forces $P(\tilde{F}_{el})$ [Fig. 1(d), with $\tilde{F}_{el} \equiv F_{el}(x)/\sigma_{F_{el}}$], which exhibits a positive skewness of 0.176. The interpretation of this is that strongly pinned points of the interface lagging behind the mean interface height give rise to a long negative tail in $P(\tilde{h})$ and a long positive tail in $P(\tilde{F}_{el})$ as the points x with negative $h(x) - \langle h \rangle$ lagging behind the rest of the interface typically experience a positive $F_{el}(x)$. These features are a consequence of the broken symmetry between parts of the interface above and below $\langle h \rangle$ due to the direction of F_{ext}, and can be reproduced also for interfaces with local and infinite-range (mean-field) interactions (Fig. 1 of Supplemental Material [20]) and for continuous-time dynamics (Fig. 3 of Supplemental Material).

Asymmetric trends in interface segments.—Next, we examine if the broken symmetry is manifested in other properties of $h(x)$ as well. To this end, we consider interface segments $h_s(x)$ of length s, i.e., we study the problem on various scales s, as a function of segment-level quantities such as $\langle h_s\rangle - \langle h\rangle$ (difference of the mean segment height and the mean interface height) and $\langle F_{\mathrm{el},s}\rangle$ (the mean elastic force acting on the segment). Figure 2(a) shows a set of ensemble-averaged scaled segment profiles $[h_s(x) - \langle h_s\rangle]/\mathrm{SD}(h_s)$ for $s = 867$ (a "large" example scale smaller than L) for different values of $\langle h_s\rangle - \langle h\rangle$ [color bar in Fig. 2(a)]. These exhibit clear, approximately parabolic trends for large values of $|\langle h_s\rangle - \langle h\rangle|$, such that the "opening direction" of the curves is toward the mean interface height. Moreover, these profiles exhibit asymmetry with respect to $\langle h\rangle$, such that there is an excess of profiles with a large negative $\langle h_s\rangle - \langle h\rangle$, shown as dashed lines in Fig. 2(a) in addition to the profiles computed with symmetric binning on both sides of $\langle h_s\rangle - \langle h\rangle = 0$ (solid lines). Moreover, comparing the symmetrically binned average segment height profiles for different $|\langle h_s\rangle - \langle h\rangle|$ and s, by computing the difference $\max(h_+) - \max(-h_-)$ [where $\max(h_+)$ refers to the maximum of the normalized average segment height profile with a positive $\langle h_s\rangle - \langle h\rangle$ and $\max(-h_-)$ is the maximum of the negative normalized average segment height profile with a negative $\langle h_s\rangle - \langle h\rangle$; only bins with more than 10 000 segments are considered here to avoid spurious effects due to statistical noise], reveals an additional signature of asymmetry: For small s, the difference is close to zero but slightly positive [pale red in Fig. 2(c)], while for large s and $|\langle h_s\rangle - \langle h\rangle|$ it becomes clearly negative [blue in Fig. 2(c)], showing that the interface segments exhibit asymmetry also for large scales, in addition to the long negative tail in the distribution $P(\tilde{h})$ of local heights in Fig. 1(c).

Analogous quantities can be studied by considering segments with different average elastic forces $\langle F_{\mathrm{el},s}\rangle$ [Figs. 2(b) and 2(d)]. Figure 2(b) shows a set of ensemble-averaged segment profiles for $s = 867$ for different values of $\langle F_{\mathrm{el},s}\rangle$ [color bar in Fig. 2(b)]. These average segment profiles are qualitatively similar to the ones found above when conditioning with the value of $\langle h_s\rangle - \langle h\rangle$, but the trends are somewhat less parabolic looking, suggesting that they may be better captured by a higher-order polynomial. Again, there is an excess of profiles with a large positive value of $\langle F_{\mathrm{el},s}\rangle$ [dashed lines in Fig. 2(b)], corresponding to segments which are lagging behind the mean height of the interface. Another difference is that for large s, $\langle F_{\mathrm{el},s}\rangle$ has a tendency to approach zero, and hence the interval of $|\langle F_{\mathrm{el},s}\rangle|$ values in Fig. 2(d) gets increasingly narrow as larger s's are considered. Nevertheless, an analogous asymmetry is seen also in Fig. 2(d), such that for small scales $\max(-h_+) - \max(h_-)$ is close to zero (+ and − now refer to positive and negative values of $\langle F_{\mathrm{el},s}\rangle$, respectively), while a clearly negative value is found for the largest s's for a given $|\langle F_{\mathrm{el},s}\rangle|$. These findings constitute a large-scale analog of the long positive tail in the distribution $P(\tilde{F}_{\mathrm{el}})$ of local elastic forces in Fig. 1(d).

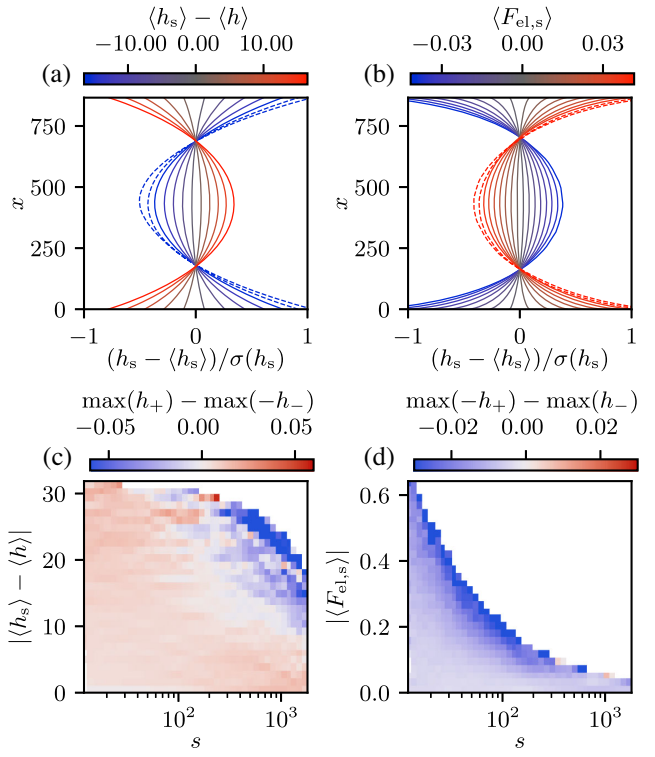

FIG. 2. (a),(b) Scaled segment profiles $[h_s(x) - \langle h_s\rangle]/\mathrm{SD}(h_s)$ for $s = 867$ averaged within bins symmetric with respect to $\langle h_s\rangle - \langle h\rangle = 0$ and $\langle F_{\mathrm{el},s}\rangle = 0$, respectively (solid lines), with the values of $\langle h_s\rangle - \langle h\rangle$ and $\langle F_{\mathrm{el},s}\rangle$ indicated by the color bars. The dashed lines illustrate the excess profiles for large negative values of $\langle h_s\rangle - \langle h\rangle$ and large positive values of $\langle F_{\mathrm{el},s}\rangle$, respectively. (c), (d) Difference between the maxima of the average scaled segment profiles with a positive and the corresponding negative value of $\langle h_s\rangle - \langle h\rangle$ and $\langle F_{\mathrm{el},s}\rangle$, respectively, for different scales s.

Scaling properties of the segments.—Next, we address the question of the scaling properties of the segments $h_s(x)$ and how these may depend on $\langle h_s\rangle - \langle h\rangle$ and $\langle F_{\mathrm{el},s}\rangle$. Given the clear trends illustrated in Figs. 2(a) and 2(b), we use DFA-n, which performs local detrending with least-squares fitting of nth degree polynomials in windows of length s. The mean squared differences from the trends are computed and averaged over all the windows to obtain the squared fluctuation function $F(s)^2$. Conventionally, the scaling exponent α is obtained by a linear fit from a logarithmic plot of $F(s) \propto s^{\alpha}$ [23,24]. Therefore, with DFA-0 the exponents α and ζ are equal [27]. We perform a scale-dependent segmentation scheme [25] to obtain scale-dependent exponents $\alpha(s)$ in short segments of the height profiles: The fluctuation function is computed in maximally overlapping windows at scales s, $s \pm 1$, and $\alpha(s)$ is obtained by central finite differences from the logarithmic quantities [25]. To achieve maximal spatial

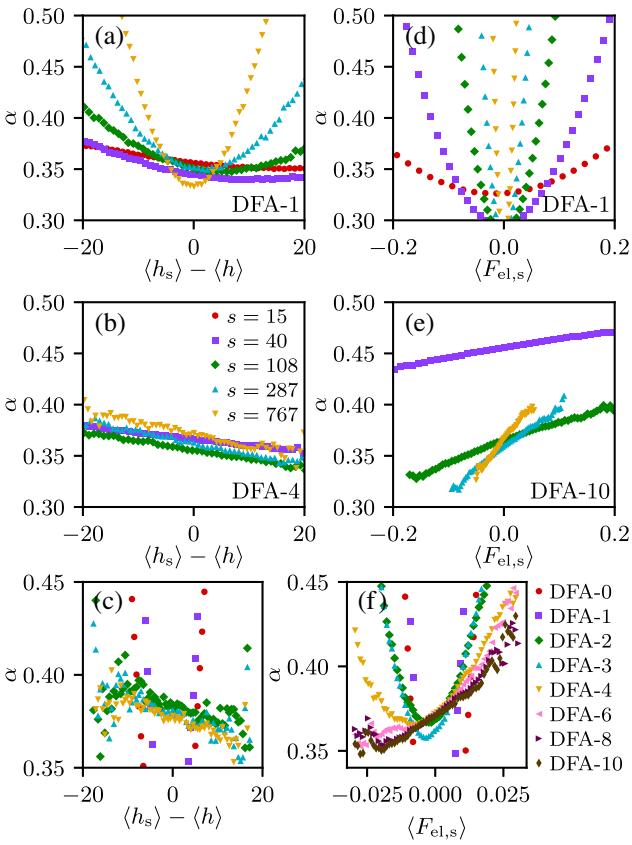

FIG. 3. (a),(b) DFA scaling exponents α for different s [legend in (b)] as a function of $\langle h_s \rangle - \langle h \rangle$ for DFA-1 and DFA-4, respectively. (c) Convergence of the α's for different DFA orders for $s = 1602$. (d)–(f) Corresponding data as a function of $\langle F_{\mathrm{el},s} \rangle$, with DFA-10 in (e).

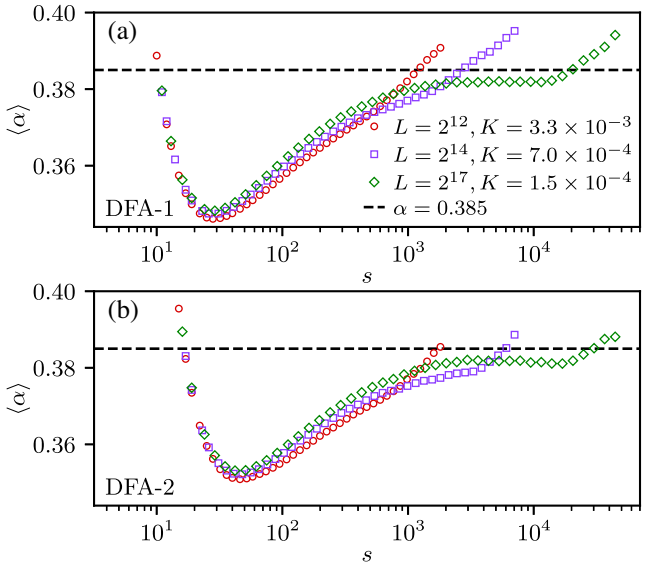

FIG. 4. Average scaling exponent $\langle \alpha \rangle$, weighted by the number of occurrences of segments with the different $\langle h_s \rangle - \langle h \rangle$ values, for different L (and K) as a function of the scale s, considering DFA-1 and DFA-2 in (a) and (b), respectively. Dashed lines indicate the literature value of the roughness exponent $\zeta \approx 0.385$.

locality for our results, we compute the fluctuation functions in segments of length $s + 1$.

Figures 3(a) and 3(d) show the scaling exponent α obtained from DFA-1 for various scales s as functions of $\langle h_s \rangle - \langle h \rangle$ and $\langle F_{\mathrm{el},s} \rangle$, respectively. These exhibit paraboliclike dependencies on $\langle h_s \rangle - \langle h \rangle$ and $\langle F_{\mathrm{el},s} \rangle$, which however are a consequence of the linear detrending not being sufficient here given the higher-order trends revealed in Figs. 2(a) and 2(b). In Figs. 3(b) and 3(e), the corresponding data are shown as obtained using higher-order polynomials for detrending [DFA-4 and DFA-10 in Figs. 3(b) and 3(e), respectively, chosen to represent the converged results]. To illustrate the convergence of the results upon increasing the DFA order, Figs. 3(c) and 3(f) show the α values for a fixed $s = 1602$ (a "large" example scale), obtained by using different orders of the detrending polynomial. In the limit of high DFA order we find a key result of this Letter, i.e., an approximately linear dependence of α on $\langle h_s \rangle - \langle h \rangle$ and $\langle F_{\mathrm{el},s} \rangle$, with the slope being negative in Figs. 3(b) and 3(c) (height difference) and positive in Figs. 3(e) and 3(f) (elastic force), showing how the broken symmetry due to the external force is manifested in the scaling properties of the interface segments. Notice how a higher-order polynomial is needed for detrending of the segments conditioned on the value of $\langle F_{\mathrm{el},s} \rangle$, consistent with the nonparabolic profiles in Fig. 2(b). We also note that for sufficiently large s (approximately for $s \gtrsim 100$), α does not exhibit any clear dependence on s, consistent with the scale-free nature of fluctuations of $h(x)$ expected at the depinning threshold. This is directly evident in Fig. 3(b) where the curves for different s approximately overlap. A similar conclusion can be reached regarding the data shown in Fig. 3(e) if one rescales the horizontal axis with the s-dependent range of $\langle F_{\mathrm{el},s} \rangle$ [not shown; see also Fig. 2(d)]. Thus, we generally find a larger α for negative $\langle h_s \rangle - \langle h \rangle$ and positive $\langle F_{\mathrm{el},s} \rangle$, i.e., for segments that are lagging behind the average interface. This is likely due to the "stretched" nature of the strongly pinned segments which are being pulled forward by the combination of F_{ext} and $\langle F_{\mathrm{el},s} \rangle$ [see also the dashed lines in Figs. 2(a) and 2(b)], resulting in stronger correlations (larger α) in such segments. Analogous results are obtained also for interfaces with local elasticity (Fig. 2 of Supplemental Material [20]) and for continuous-time dynamics (Fig. 4 of Supplemental Material).

Finally, we consider the relation of these local, segment-level exponents α and the global roughness exponent ζ. To this end, in Fig. 4, we consider the average of the $(\langle h_s \rangle - \langle h \rangle)$-dependent DFA scaling exponent $\langle \alpha \rangle$, weighted by the number of occurrences of the different $\langle h_s \rangle - \langle h \rangle$ values in the dataset, which equals the average of α of segments of a given s. Figures 4(a) and 4(b) show the resulting $\langle \alpha \rangle$'s as a function of the scale s for different system

sizes (with the K parameter adjusted so that the correlation length along the interface remains roughly the same fraction of L for different L), considering DFA-1 and DFA-2, respectively. In the limit of large s, $\langle\alpha\rangle$ converges to a value very close to $\zeta \approx 0.385$ (dashed lines in Fig. 4) largely independently of the DFA order (the increase of $\langle\alpha\rangle$ for the very largest s's is likely due to the K-dependent correlation length). Thus, the global roughness exponent emerges on large scales as an average of the local, $(\langle h_s\rangle - \langle h\rangle)$-dependent scaling exponents.

Conclusions.—To conclude, our results show that F_{ext} breaks the symmetry of roughness with respect to $\langle h\rangle$ of elastic interfaces in random media at the depinning threshold, suggesting that a single roughness exponent ζ is not a full description of their rough morphology, and that the spectrum of local, segment-level exponents needs to be considered as well. We emphasize that this result applies for all ranges of the elastic interactions, and is true already on the level of *individual* interface configurations, and hence this result significantly adds to previous studies arguing that distributions $P(w^2)$ of the interface width are needed in addition to ζ to characterize *ensembles* of rough interface configurations [28]. Our results might be relevant for related problems like the scaling properties of anisotropic fracture surfaces [29], and call for experimental studies of diverse systems ranging from domain walls in ferromagnetic thin films [30] to planar crack fronts [31]. Finally, an interesting avenue for future work would be to check if the asymmetry persists in the thermally activated creep regime governed by the equilibrium roughness exponent [32].

*esko.toivonen@tuni.fi

[1] S. Zapperi, P. Cizeau, G. Durin, and H. E. Stanley, Dynamics of a ferromagnetic domain wall: Avalanches, depinning transition, and the Barkhausen effect, Phys. Rev. B **58**, 6353 (1998).

[2] P. Paruch, T. Giamarchi, and J.-M. Triscone, Domain Wall Roughness in Epitaxial Ferroelectric $PbZr_{0.2}Ti_{0.8}O_3$ Thin Films, Phys. Rev. Lett. **94**, 197601 (2005).

[3] J. Joanny and P.-G. De Gennes, A model for contact angle hysteresis, J. Chem. Phys. **81**, 552 (1984).

[4] L. Laurson, X. Illa, S. Santucci, K. T. Tallakstad, K. J. Måløy, and M. J. Alava, Evolution of the average avalanche shape with the universality class, Nat. Commun. **4**, 2927 (2013).

[5] P. Chauve, T. Giamarchi, and P. Le Doussal, Creep and depinning in disordered media, Phys. Rev. B **62**, 6241 (2000).

[6] T. Nattermann, S. Stepanow, L.-H. Tang, and H. Leschhorn, Dynamics of interface depinning in a disordered medium, J. Phys. II (France) **2**, 1483 (1992).

[7] A. Rosso, P. Le Doussal, and K. J. Wiese, Avalanche-size distribution at the depinning transition: A numerical test of the theory, Phys. Rev. B **80**, 144204 (2009).

[8] A. Rosso and W. Krauth, Roughness at the depinning threshold for a long-range elastic string, Phys. Rev. E **65**, 025101(R) (2002).

[9] O. Duemmer and W. Krauth, Depinning exponents of the driven long-range elastic string, J. Stat. Mech. (2007) P01019.

[10] S. Zapperi and M. Zaiser, Depinning of a dislocation: The influence of long-range interactions, Mater. Sci. Eng. A **309**, 348 (2001).

[11] V. Mohles, D. Rönnpagel, and E. Nembach, Simulation of dislocation glide in precipitation hardened materials, Comput. Mater. Sci. **16**, 144 (1999).

[12] B. Bakó, D. Weygand, M. Samaras, W. Hoffelner, and M. Zaiser, Dislocation depinning transition in a dispersion-strengthened steel, Phys. Rev. B **78**, 144104 (2008).

[13] A. Tanguy, M. Gounelle, and S. Roux, From individual to collective pinning: Effect of long-range elastic interactions, Phys. Rev. E **58**, 1577 (1998).

[14] H. Gao and J. R. Rice, A first-order perturbation analysis of crack trapping by arrays of obstacles, J. Appl. Mech. **56**, 828 (1989).

[15] J. Schmittbuhl, S. Roux, J.-P. Vilotte, and K. J. Måløy, Interfacial Crack Pinning: Effect of Nonlocal Interactions, Phys. Rev. Lett. **74**, 1787 (1995).

[16] S. Ramanathan and D. S. Fisher, Dynamics and Instabilities of Planar Tensile Cracks in Heterogeneous Media, Phys. Rev. Lett. **79**, 877 (1997).

[17] L. Laurson, S. Santucci, and S. Zapperi, Avalanches and clusters in planar crack front propagation, Phys. Rev. E **81**, 046116 (2010).

[18] D. Bonamy, S. Santucci, and L. Ponson, Crackling Dynamics in Material Failure as the Signature of a Self-Organized Dynamic Phase Transition, Phys. Rev. Lett. **101**, 045501 (2008).

[19] P. Moretti, M.-Carmen Miguel, M. Zaiser, and S. Zapperi, Depinning transition of dislocation assemblies: Pileups and low-angle grain boundaries, Phys. Rev. B **69**, 214103 (2004).

[20] See Supplemental Material at http://link.aps.org/supplemental/10.1103/PhysRevLett.129.175701 for additional material supporting the conclusions of the main text, which includes Refs. [21,22].

[21] E. E. Ferrero, S. Bustingorry, and A. B. Kolton, Nonsteady relaxation and critical exponents at the depinning transition, Phys. Rev. E **87**, 032122 (2013).

[22] A. Rosso, A. K. Hartmann, and W. Krauth, Depinning of elastic manifolds, Phys. Rev. E **67**, 021602 (2003).

[23] C.-K. Peng, S. V. Buldyrev, S. Havlin, M. Simons, H. E. Stanley, and A. L. Goldberger, Mosaic organization of DNA nucleotides, Phys. Rev. E **49**, 1685 (1994).

[24] J. W. Kantelhardt, E. Koscielny-Bunde, H. H. Rego, S. Havlin, and A. Bunde, Detecting long-range correlations with detrended fluctuation analysis, Physica (Amsterdam) **295A**, 441 (2001).

[25] M. Molkkari, G. Angelotti, T. Emig, and E. Räsänen, Dynamical heart beat correlations during running, Sci. Rep. **10**, 13627 (2020).

[26] F. Elías, A. B. Kolton, and K. J. Wiese, Depinning and flow of a vortex line in a uniaxial random medium, Phys. Rev. B **105**, 224209 (2022).

[27] The least-squares fit of a zeroth-order polynomial is equal to the mean, and hence the mean squared differences become variances. We also omit the integration step usually performed in DFA, as the height profile is already considered a random walk and not its steps.
[28] A. Rosso, W. Krauth, P. Le Doussal, J. Vannimenus, and K. J. Wiese, Universal interface width distributions at the depinning threshold, Phys. Rev. E **68**, 036128 (2003).
[29] L. Ponson, D. Bonamy, and E. Bouchaud, Two-Dimensional Scaling Properties of Experimental Fracture Surfaces, Phys. Rev. Lett. **96**, 035506 (2006).
[30] L. J. Albornoz, P. C. Guruciaga, V. Jeudy, J. Curiale, and S. Bustingorry, Domain-wall roughness in GdFeCo thin films: crossover length scales and roughness exponents, Phys. Rev. B **104**, 024203 (2021).
[31] S. Santucci, M. Grob, R. Toussaint, J. Schmittbuhl, A. Hansen, and K. Maløy, Fracture roughness scaling: A case study on planar cracks, Europhys. Lett. **92**, 44001 (2010).
[32] E. E. Ferrero, L. Foini, T. Giamarchi, A. B. Kolton, and A. Rosso, Creep motion of elastic interfaces driven in a disordered landscape, Annu. Rev. Condens. Matter Phys. **12**, 111 (2021).